

Northumbria Research Link

Citation: Li, Teng, Zhang, Baogang, Cheng, Xiao, Westoby, Matt, Li, Zhenhong, Ma, Chi, Hui, Fengming, Shokr, Mohammed, Liu, Yan, Chen, Zhuoqi, Zhai, Mengxi and Li, Xinqing (2019) Resolving Fine-Scale Surface Features on Polar Sea Ice: A First Assessment of UAS Photogrammetry Without Ground Control. *Remote Sensing*, 11 (7). p. 784. ISSN 2072-4292

Published by: MDPI

URL: <https://doi.org/10.3390/rs11070784> <<https://doi.org/10.3390/rs11070784>>

This version was downloaded from Northumbria Research Link:
<http://nrl.northumbria.ac.uk/39051/>

Northumbria University has developed Northumbria Research Link (NRL) to enable users to access the University's research output. Copyright © and moral rights for items on NRL are retained by the individual author(s) and/or other copyright owners. Single copies of full items can be reproduced, displayed or performed, and given to third parties in any format or medium for personal research or study, educational, or not-for-profit purposes without prior permission or charge, provided the authors, title and full bibliographic details are given, as well as a hyperlink and/or URL to the original metadata page. The content must not be changed in any way. Full items must not be sold commercially in any format or medium without formal permission of the copyright holder. The full policy is available online: <http://nrl.northumbria.ac.uk/policies.html>

This document may differ from the final, published version of the research and has been made available online in accordance with publisher policies. To read and/or cite from the published version of the research, please visit the publisher's website (a subscription may be required.)

www.northumbria.ac.uk/nrl



Article

Resolving Fine-Scale Surface Features on Polar Sea Ice: A First Assessment of UAS Photogrammetry Without Ground Control

Teng Li ^{1,2,3,4} , Baogang Zhang ^{1,3,4} , Xiao Cheng ^{1,3,4,*} , Matthew J. Westoby ² , Zhenhong Li ⁵ , Chi Ma ^{1,3}, Fengming Hui ^{1,3,4}, Mohammed Shokr ⁶ , Yan Liu ^{1,3,4}, Zhuoqi Chen ^{1,3,4}, Mengxi Zhai ^{1,3,4} and Xinqing Li ^{1,3,4} 

¹ State Key Laboratory of Remote Sensing Science, College of Global Change and Earth System Science (GCESS), Beijing Normal University, Beijing 100875, China; litengbnu@foxmail.com (T.L.); zhang_bob@bnu.edu.cn (B.Z); machi63269@126.com (C.M.); huifm@bnu.edu.cn (F.H.); lyxixi_2003@163.com (Y.L.); chenzq@bnu.edu.cn (Z.C.); Mengxi.zhai@mail.bnu.edu.cn (M.Z); lixinqing0710@163.com (X.L.)

² Department of Geography and Environmental Sciences, Engineering and Environment, Northumbria University, Newcastle upon Tyne NE1 8ST, UK; matt.westoby@northumbria.ac.uk

³ Joint Center for Global Change Studies (JCGCS), Beijing 100875, China

⁴ University Corporation for Polar Research (UCPR), Beijing 100875, China

⁵ School of Engineering, Newcastle University, Newcastle upon Tyne NE1 7RU, UK; zhenhong.li@ncl.ac.uk

⁶ Science and Technology Branch, Environment Canada, Toronto, ON M3H5T4, Canada; mo.shokr.ms@gmail.com

* Correspondence: xcheng@bnu.edu.cn

Received: 18 February 2019; Accepted: 28 March 2019; Published: 1 April 2019



Abstract: Mapping landfast sea ice at a fine spatial scale is not only meaningful for geophysical study, but is also of benefit for providing information about human activities upon it. The combination of unmanned aerial systems (UAS) with structure from motion (SfM) methods have already revolutionized the current close-range Earth observation paradigm. To test their feasibility in characterizing the properties and dynamics of fast ice, three flights were carried out in the 2016–2017 austral summer during the 33rd Chinese National Antarctic Expedition (CHINARE), focusing on the area of the Prydz Bay in East Antarctica. Three-dimensional models and orthomosaics from three sorties were constructed from a total of 205 photos using Agisoft PhotoScan software. Logistical challenges presented by the terrain precluded the deployment of a dedicated ground control network; however, it was still possible to indirectly assess the performance of the photogrammetric products through an analysis of the statistics of the matching network, bundle adjustment, and Monte-Carlo simulation. Our results show that the matching networks are quite strong, given a sufficient number of feature points (mostly > 20,000) or valid matches (mostly > 1000). The largest contribution to the total error using our direct georeferencing approach is attributed to inaccuracies in the onboard position and orientation system (POS) records, especially in the vehicle height and yaw angle. On one hand, the 3D precision map reveals that planimetric precision is usually about one-third of the vertical estimate (typically 20 cm in the network centre). On the other hand, shape-only errors account for less than 5% for the X and Y dimensions and 20% for the Z dimension. To further illustrate the UAS's capability, six representative surface features are selected and interpreted by sea ice experts. Finally, we offer pragmatic suggestions and guidelines for planning future UAS-SfM surveys without the use of ground control. The work represents a pioneering attempt to comprehensively assess UAS-SfM survey capability in fast ice environments, and could serve as a reference for future improvements.

Keywords: landfast sea ice; unmanned aerial system (UAS); Antarctic expedition; structure from motion (SfM); surface features; photogrammetry

1. Introduction

Landfast sea ice (or ‘fast ice’) forms attached to a coastline, island, grounded ridge, or an iceberg [1,2] and, in this sense, can be distinguished from ‘drift’ sea ice. It is the dominant cryospheric composition of the near-shore zone. Furthermore, as a ubiquitous feature of the Antarctic coastal zone, fast ice serves as a sensitive indicator and modulator of Antarctic climate processes [3] and, as a structural element of the Antarctic ice shelf, integrity and marine ecosystem sustainability [4].

Although landfast sea ice is an important component of the Antarctic sea ice cover, many processes associated with its formation, dynamical behaviour, and decay remain poorly understood [5,6], especially at the local scale, as direct observations are scarce and challenging to obtain. Small-scale deformations of fast ice, ranging from dozens to a few hundred metres, manifest as forms of fracturing, rafting, ridging, and rubble ice fields. Similar to small-scale pressure ridges, which regulate the air and water drag coefficients, and are therefore of geophysical interest, deformation information acts as an critical input to regional ice-ocean-atmosphere interaction models [7]. Although it can be interpreted from declassified satellite imagery, in general, an in-depth understanding of the role of landfast sea ice in natural and human systems has been limited by a lack of reliable data. The possible utility of high-resolution optical satellite imagery for sea ice monitoring has been suggested through visual inspection [8]. These data cannot, however, provide a detailed characterization of sea ice surface topography, and possess substantial uncertainty due to ambiguity in spectral unmixing [9]. Currently, it is still a challenge for the available satellite systems in the aspects of timeliness and resolution.

Taking full advantage of centimetre-scale aerial imagery, Lu et al. [8] analyzed aerial photographs of Arctic summer sea ice obtained during the Third Chinese National Arctic Research Expedition in 2008 (CHINARE2008). Likewise, Landy et al. [10,11] parameterized surface ice roughness by terrestrial LiDAR (Light Detection And Ranging) at a similar scale. Although increasingly applied to acquire high-resolution fast ice scenes in near-real time, airborne photogrammetry is still logistically challenging and cost-prohibitive.

Advances in unmanned aerial system (UAS) technology and the sophistication and accessibility of computer vision-based digital photogrammetry, commonly termed structure from motion (SfM) with multi-view stereo (MVS), are rapidly enhancing our ability to measure and understand geophysical phenomena [12]. Such technologies achieve a flexible compromise between high temporal resolution and broad spatial coverage, hence they are bridging the gap between sporadic ground-based measurements and coarse space-borne remote sensing by enabling efficient and affordable observations at both high spatial and temporal resolution [13–15]. Such methods have already exhibited satisfactory performance in a variety of challenging natural scenarios [16,17], including in various cryospheric fields. These methods have opened up new opportunities for snow and ice research [18]. It is worth noting that Dammann et al. [19] also made use of LiDAR to validate their fast ice surface roughness derived from an UAS survey. The results from the two datasets are in line with each other, implying that digital surface models (DSM) derived from UAS-SfM capture the full spectrum of relief variations.

UAS-SfM methods appear to be a promising tool for tackling observational barriers in sea ice research. The uptake of UAS technology for Antarctic-related research is demonstrable [20–22]. Of the 18 published papers in a non-exhaustive review conducted in Leary [23], only three projects were directly associated with sea ice, yet none were concerned with fast ice research. The very first attempt among similar studies appeared more than ten years ago, where researchers from the British Antarctic Survey (BAS) used a 6 kg fixed-wing UAS to measure air temperatures at very low altitudes over the Weddell Sea [24]. The remaining two studies comprised ship-based work: One conducted on board the R/V Nathaniel B. Palmer of the U.S., and the other on board the RSV Aurora Australis of the Australia Antarctic Division (AAD). The former case utilized two testing models, a DJI Phantom 2 Vision+ quadcopter and a more advanced eight-rotor S1000 to determine floe size distribution [25]; the latter project was initiated for icebreaker navigation. When passing through sea with a high ice concentration, the quadcopter and fixed-wing were valuable additions to the current suite of sea ice navigation

tool kits [26]. However, their models still suffered from unstable batteries, and a comprehensive photogrammetric assessment is still lacking. In the present study we try to address such problems.

Due to the low-contrast surface of snow and ice, compared with other natural or artificial scenes, previous research has suggested that the robust key-point extraction and matching of stereo image pairs is difficult, if not impossible, using traditional algorithms [27]. One would assume that an undeveloped surface texture over sea ice, combined with sub-optimal illumination conditions at high latitudes, might produce images that are unsuitable for developing valid stereo pairings [28]. Nonetheless, the matching performance and precision evaluation of photogrammetric products from UAS on sea ice remains under-developed. Normally, spatially well-distributed ground control points (GCPs) serve as an independent check for photogrammetrically-derived orthomosaics and DSMs [29–31]. More recently, the maturation of real-time-kinetic (RTK) and differential technology has enabled onboard GNSS (Global Navigation Satellite System)-supported UAS surveys to achieve almost the same accuracy [32]. However, these approaches either require arduous on-foot measurements, or prohibitively expensive segments. Especially with regard to the stability of fast ice, tidal cracks, melting, or deformation would mechanically weaken the ice [33,34], which could cause potential fatalities if the surveyors are not familiar with the environmental setting. In addition, icebergs or large floes could also tumble, threatening the safety of the personnel and vehicles [35]. In other words, walkover surveys are usually impractical and unsafe. It is not just difficult but, indeed, perilous to deploy ground control over given unstable fast ice. From the standpoint of photogrammetry, here we circumvent the conventional manner and explore a safer and potentially photogrammetrically effective method for evaluating the relative precision of photogrammetric products derived without ground control through an assessment of matching network strength, exterior orientation, and perturbation statistics [36].

The following paper is organized as follows: Section 2 introduces the study site; Section 3 describes the UAS model, the source data acquisition, and the subsequent processing steps; we analyze the photogrammetric products and evaluate their precision in Section 4. Finally, Section 5 sheds light on methodological deficiencies and possible future developments, followed by a brief summary of the work in Section 6. To our best knowledge, the present study represents the first assessment of direct georeferencing-based UAS-SfM, in a sea ice environment.

2. Study Site

Situated in Princess Elizabeth Land in southeast Antarctica, Zhongshan (69°22'S , 76°22'E) is a Chinese research station, which was constructed in 1989. It lies on the eastern rim of the Prydz Bay, on a relatively shallow but widespread continental shelf extending into the Indian Ocean (see Figure 1). The study area is separated from the Antarctic plateau by the low-lying Larsemann Hills, protecting it largely from immediate katabatic winds from the north-east. Locally-documented extreme wind speeds can reach $40 \text{ m}\cdot\text{s}^{-1}$. In the austral summer, the air temperature fluctuates between $-10 \text{ }^{\circ}\text{C}$ and $5 \text{ }^{\circ}\text{C}$; during December, inclement weather conditions (such as fogging and snowfall) are common, and the mean temperature is $0.17 \text{ }^{\circ}\text{C}$.

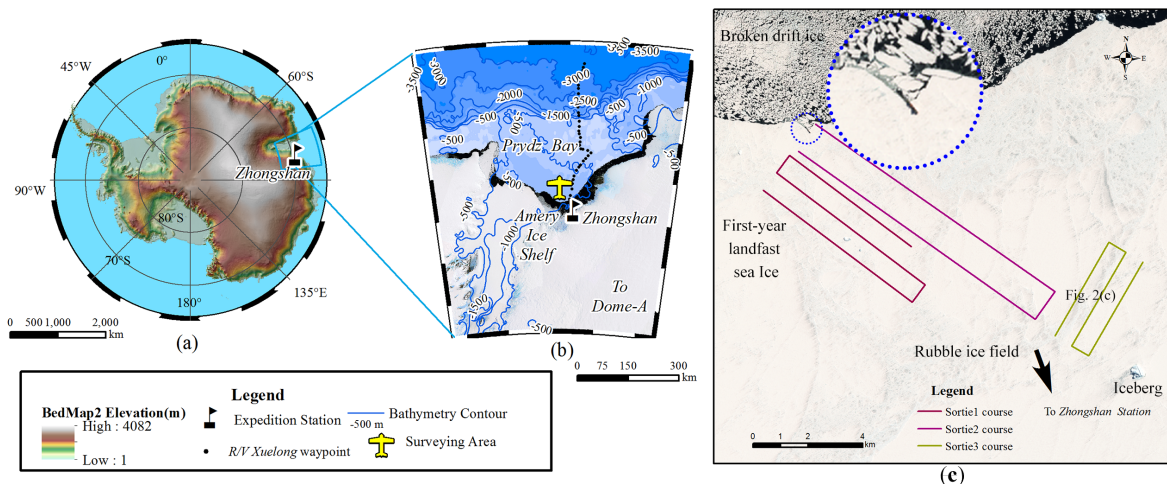


Figure 1. Study site and Chinese Antarctic expedition settings. (a) The location of the Chinese flagship scientific research station, Zhongshan, in east Antarctica, overlaid on the Bedmap2 Antarctic ice sheet surface elevation map. (b) The coastal environment near Zhongshan station. In November each year, R/V Xuelong usually traverses through westerlies and the drift ice zone of the Prydz Bay to approach and re-supply the polar expedition team. The landfast sea ice near shore often extends 30–40 km from the Larsemann Hills. The background Antarctic ice sheet mosaic is the LIMA from USGS. (c) The programmed path of three missions. Note the dashed circle close-up in upper part: The Sentinel-2 optical satellite happened to capture the moment on 29 November 2016, when the R/V Xuelong (black linear feature) was trying to break the outer boundary and pierce into the landfast ice. It was held still a few kilometres past that position, and then anchored there.

This area also serves as a navigation channel and anchoring point for Chinese icebreakers to access Zhongshan Station to exchange personnel and resupply for expeditions at the end of November or early December, when the one-year-old fast ice is widely distributed around the station [37,38]. Cargo transportation by heavy snow tractors and various kinds of scientific research activities occur on the surface of the nearshore fast ice; the area is, therefore, of logistical interest. Locally, fast ice can detach from the land in early summer as a result of coincident strong winds, periodical spring tides, penetrating ocean swells, or a combination of these factors, increasing the risk to life. The complete annual cycle of landfast sea ice growth and decaying processes near to Zhongshan was first recorded by Lei et al. [39], as part of the Antarctic Fast-Ice Network (AFIN) initiative [40]. Fast ice grows from mid-February to late November, reaching a maximum thickness of 1.6–1.8 m, covered by a layer of snow of variable depth. Beyond late November, the ice begins to decay by rapid disintegration, combined with surface melting. Interestingly, ridges and bergy bits were found to influence the local ice properties significantly [39].

3. Data and Methods

In recent years, UAS have become more affordable and dramatically easier to operate, allowing end users from various fields to focus on integrating specific sensors and the collection of data [18]. For operation in Antarctica, unique design specifications have to be taken into consideration, in light of the low temperatures, strong winds, and complex logistical arrangements. Further, weak illumination (caused by low solar altitude), and image over-exposure (caused by highly reflective snow and ice surfaces) may complicate regular photogrammetric processing. To address these concerns in a cost-effective way, we propose a series of solutions, which we explain below.

3.1. UAS Model Specification

The Polar Hawk-III is a fixed-wing UAS with an integrated remote sensing system. The UAS was jointly designed, developed, and implemented by Feima Robotics Laboratory and Beijing Normal University. It has a wing span of 1.6 m, weighs ~3.3 kg and costs ~6500 U.S. dollars. Its main

architecture is outlined in Figure 2a and is comprised mostly of commercial, off-the-shelf components; the system is also fully modular, for ease of transport.

The framework is made of Carbon Fiber Composites (CFCs) with an Expanded PolyOlefin (EOP) material covering the fuselage, which absorbs a significant amount of vibration. A brushless electric motor provides propeller thrust. To minimize rotational variations, a 3-axis accelerometer and gyroscope controls self-stabilization. The model is resistant to wind, up to $12 \text{ m}\cdot\text{s}^{-1}$. Deployment is by pilot casting (see Figure 2b); whereas, for landing, both parachuting or glided landing options are available.

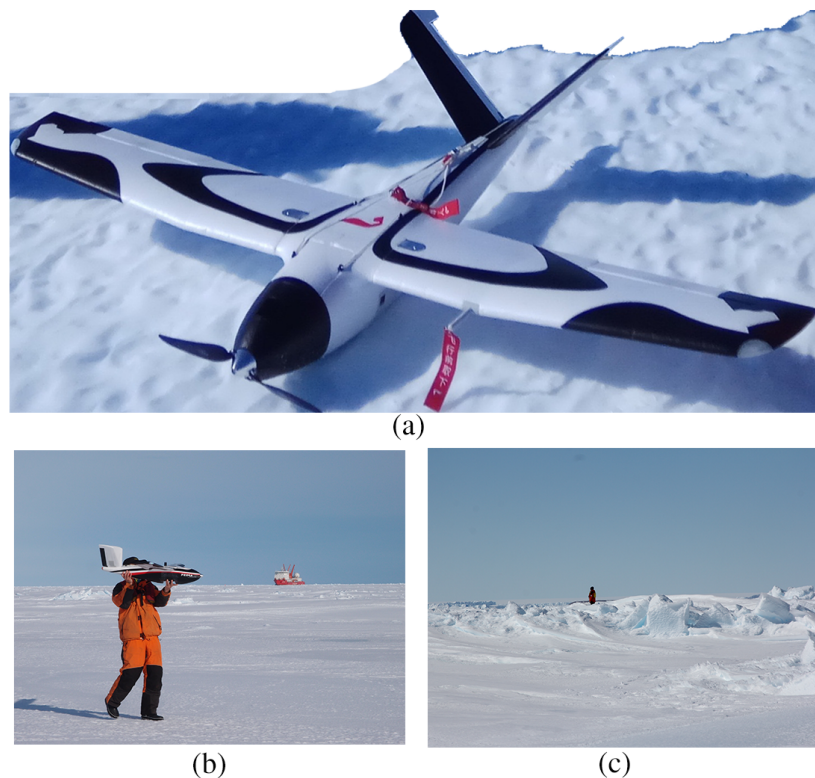


Figure 2. UAS model illustration and field work scenes. (a) *Polar Hawk-III* model. Refer to Section 3.1 for the model's detailed specifications. (b) Holding the model, the operator is about to cast it into air to deploy the vehicle. Note the R/V Xuelong, 400 m in the background. (c) A photo of a small area of rough ice. The stiff ice floes stand out chaotically, up to about 0.5~1 m. Please refer to the person (height: 1.75 m) behind for physical scale.

The UAS is propelled by a tailored lithium polymer battery with an overall power of 9800 mAh, permitting a sortie length of 1.5 h at a cruising speed of $60 \text{ km}\cdot\text{h}^{-1}$. To maximize battery life (and, thus, flight times), we warmed the batteries in thermal insulation blankets, prior to use.

Aerial images are retrieved by a full-frame SONY DSC-RX1R II camera, mounted in the belly payload. The Zeiss Sonnar T*FE F2.8 len ($35.9 \times 24 \text{ mm}$) has a fixed focal length of 35 mm, and captures photos in JPEG format at a resolution of 42 megapixels (7952×5304). The instantaneous field of view (IFOV) of each exposure is dependent on relative altitude; for example, a ground sampling distance (GSD) of 10 cm is achieved at a flying height of $\sim 760 \text{ m}$. A flight control unit records the onboard GPS and IMU (Inertial Measurement Unit) data during flight missions and are linked to the camera shutter; when the shutter is triggered, the external camera position and orientation are recorded in a global geographic coordinate system simultaneously.

The vehicle is linked to a ground station by radio communication with frequency $818 \pm 15 \text{ MHz}$, up to an effective maximum radius of 15 km. The flight path is pre-programmed using a flight-planning software and, once deployed, the UAS is controlled by an autopilot, with an emergency 'return to home' functionality, in case of sustained ground station signal loss.

3.2. Data Acquisition

A large area (more than 100 km²) of fast ice with distinctive surface structures were identified from Sentinel-2A satellite imagery, at the time of the R/V Xuelong's arrival in Prydz Bay on 29 November 2016. The MSI onboard the Sentinel-2A has 12 bands, and the RGB composite of this image was used to support mission planning through visual inspection (see Figure 1c). We sought a GSD of 20 cm, as this represented an appropriate compromise between spatial coverage and surface detail representation, equivalent to a UAS flying altitude of ~1500 m above sea level and producing an image with a ground footprint of 1480 × 990 m.

To avoid motion blurring and over-exposure, key camera parameters were set, as follows: Shutter speed, 1/1600 s; aperture, 5.6; and ISO, 100~400. White balance was set to automatic and, therefore, the colour intensity of the image would be scaled based upon the amount of light and dark pixels in a given capture [41]. We manually regulated the image focus immediately before each sortie, according to the current light intensity. Our flight design incorporated respective forward and side overlaps of 80% and 60%, in line with published recommendations [42,43].

We undertook the first sortie at midnight, when the solar altitude was at its lowest (1.48°). The take-off and landing sites were located on stable sea ice, 400 m south of the mooring position of the R/V Xuelong (Figure 2b). More than 20 km² of fast ice cover was surveyed by 87 photos, in a flight lasting 45 min. We launched a second sortie (sortie-2) ~6 h later (Table 1); however, the UAS suffered an intermittent loss of contact with the ground station, forcing an end to the sortie; this sortie retrieved 56 photos, of which 53 were deemed suitable for photogrammetric use (Table 1). Three days of adverse weather between 3 December (sortie-2) and 7 December (sortie-3) hindered outdoor activities. For sortie-3, we shifted our attention to an area of landfast sea ice ~13 km southeast of the R/V Xuelong, characterized by extensive ridges measuring 0.7–0.8 m in height (Figure 2c). All in-situ records, including flight information and environmental factors, are summarized in Table 1.

Table 1. In-situ records of three (UAS) flights.

Mission No.	Date	Flight Time *			Photos
		Taking-Off	Landing	Duration (min)	
sortie-1	2 December 2016	23:31	00:15	44	87
sortie-2	3 December 2016	06:38	07:17	39	56 (53) [§]
sortie-3	7 December 2016	06:52	07:54	62	62 (60)
Mission No.	Coordinates	Height (m)	Strip	Range (km)	Area (km ²)
sortie-1	76.132°E, 69.105°S	1557	3	27.81	21.58
sortie-2	76.143°E, 69.107°S	1557	1	24.21	20.29
sortie-3	76.182°E, 69.111°S	1383	3	36.75	12.39
Mission No.	Environment Parameters †				
	Weather	Solar Altitude (°)	Temperature (°C)	Wind Speed (m·s ⁻¹)	Wind Direction
sortie-1	Clear	1.48~1.76	−5.2~−3.8	4~7	south by west
sortie-2	Clear	25.5~29.1	−4.3~−2.6	~5	south by west
sortie-3	Low Cloud	26.8~33.5	−3.6~−2.2	6~10	east

* Local time zone, which is East-5; [§] The number in parenthesis indicates the valid photos imported into PhotoScan; [†] Measured at the taking-off and landing location, maybe dozens of kilometres away from the actually vehicle.

3.3. Data Processing

We undertook SfM-MVS processing in Agisoft® PhotoScan software v1.2.4. The blurred images were eliminated, manually, to avoid matching failures (Table 1). Following image key-point extraction and an initial alignment, a self-calibrating bundle iteratively solves for the interior and external camera and scene geometry, generating a sparse 3D point cloud (of 'high' quality). If georeferenced topographic data products are desired, a common workflow comprises software-guided placement of GCPs, allowing the projection of the data into a real-world coordinate system. Alternatively,

on-board positioning information can be used in place of, or alongside with, ground control for project georeferencing. In the absence of ground control, we employed on-board GPS and IMU information to georeference our data. Non-linear geometric distortions were corrected through a self-calibrating optimization of the camera model distortion parameters, including focal length, principle coordinates, aspect ratio, skew coefficient, third order of radial distortion coefficient, and second order of tangential distortion coefficient. The sparse clouds were manually filtered, followed by a densification using an MVS algorithm to generate the dense point cloud of the fast ice surface (again, of ‘high’ quality). The dense point cloud was used to construct a DSM, from which an orthomosaic image was created at a 20 cm pixel resolution. All outputs were mapped into the WGS84-UTM43S (EPSG: 32743) projection. To maintain the visual integrity of the original imagery, the colour balancing option when exporting the orthomosaic was not checked. A more in-depth description of the workflow above can be found in [30].

To examine the image network geometry and strength in the absence of a ground control, we flexibly manipulated our PhotoScan project using the in-built Python scripting API (Application Program Interface). Following an initial alignment, images with more than three matches were extracted. To analyze the geometry network strength, we extracted the number of feature points (key-points) in each exposure position, and the amount of valid links (tie-points) between each of the stereo pairs. Moreover, to make full use of the residuals of the holistic bundle adjustment, the statistics of six exterior parameters along the courses were inspected after orientation optimization.

Point precision assessment was carried out using Monte-Carlo approaches, implemented in the MATLAB-based SfM_georef toolkit [12]. The software includes functionality to evaluate point cloud precision, and its principle is fully described in James et al. [36]. By iteratively and randomly adjusting camera model parameters using a Gaussian distribution, each point in the sparse cloud would migrate in 3D space around its original coordinates (i.e., the original (x,y,z) location before the Monte-Carlo analysis). The magnitude of point migration can be regarded as the proxy of product precision [36]. To amount for the above statistics of the exterior orientation, the mean standard deviations of position and orientation residuals were initialized as the representative perturbation for 5000 times. The total error was partitioned into two components: The portion induced from internal image network, and the portion induced from external POS records. Our Python scripts and data are available in the Supplementary Materials. All processing steps were summarized in Figure 3.

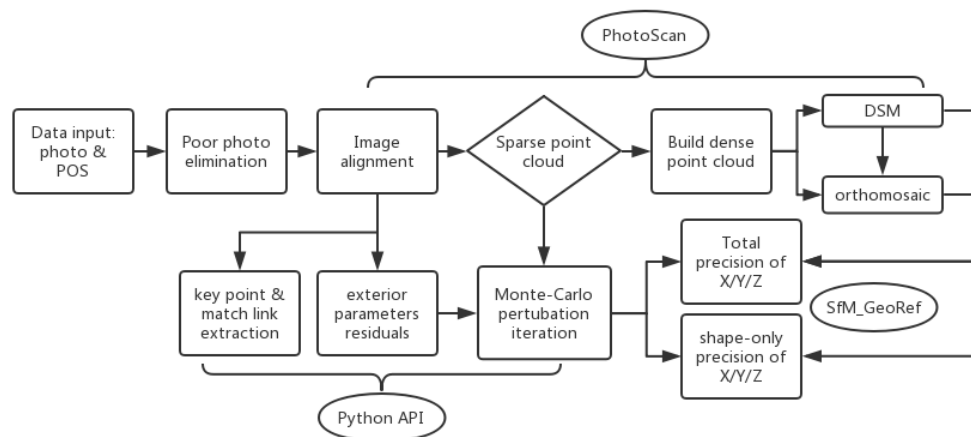


Figure 3. Flowchart of data processing.

4. Results and Interpretation

The orthomosaics and DSMs corresponding to our three sorties are shown in Figure 4a,b, respectively. At first glance, the contrast in the scene exposures is striking: For sortie-1, the darker tone results from a low solar altitude; while, for sortie-3, clouds may have reduced the surface reflectance. Two operators and the ground station can also be clearly identified in the sortie-2 orthomosaic.

With regard to the appearance of the DSM (Figure 4b), the elevation patterns are spatially complex: Peripheral areas exhibit low relative elevations, likely due to the reduced image matching success, and suggests the presence of a systematic radial bias (the so-called ‘dome effect’), superimposed by high-frequency longitudinal dithering. From these data, it is difficult to discern the actual surface topography, which was comprised of weathered snow and rough ridges on the ice surface.

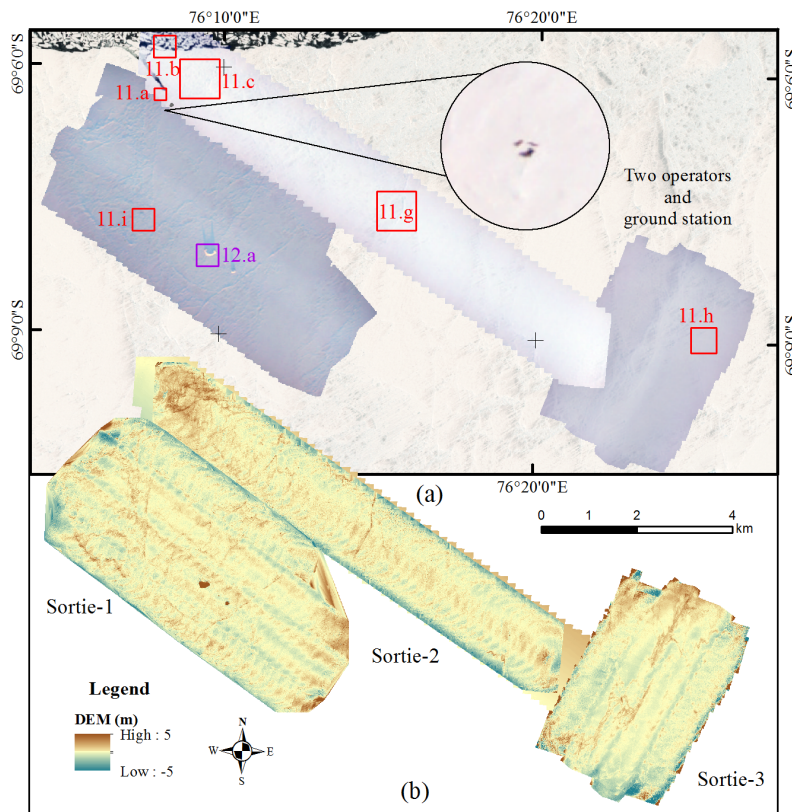


Figure 4. The standard products of the structure from motion (SfM) software, exported from Agisoft® PhotoScan v1.2.4: (a) The mosaic images after ortho-rectification. The darker tone in the sortie-1 orthomosaic is due to the lower solar altitude angle, as compared with that of sortie-2 and sortie-3. The circular close-up shows two operators and the ground station in a flat area 400 m ahead of the R/V Xuelong. See Figure 2b,c for the in-situ environment. (b) The digital surface models (DSM) of three sortie projects. Note that systematic biases include the slight ‘dome effect’ and high frequency jitters along the flight course. Please refer to Figure 1c for their respective flight courses and geographic locations.

4.1. Image Network Geometry

In more ‘traditional’ digital photogrammetric workflows, such as those employed by Impho or ERDAS LPS, operator intervention, including manual image tie-point identification, is indispensable for quality control. In contrast, the SfM method, as employed by PhotoScan, involves automatic image network reconstruction from a far greater number of feature points (often tens of thousands) and corresponding matches (often thousands). Generally speaking, a higher number of image key-points and tie-points leads to increased stability of the camera and scene geometry network.

The matching network geometry of sortie-3 is illustrated in Figure 5. Out of 60 images, 48 possessed over 20,000 key-points. The minimum number of image key-points in a single image exceeds 7000; this number might be taken as representative of images of ‘featureless’ sea ice. Images with a higher number of feature points were typically retrieved from the central part of the study area, but we also noticed that the left strip images returned more points than images in the right strip (Figure 5a); the number of tie-point matches ranged from 200 to 3100 for photos at equivalent distances in the right and

left strips, respectively. Similar patterns appear in Figure 5b. Adjacent image pairs, either in forward or sideward positions, possessed over 1500 valid matches. For their respective instance, see Figure 5c,d. Our key-point matching success rate of 85% ($\approx 1326/1569 \approx 550/634$) indicates sufficient robustness, although the number of tie-point matches in our projects never reached the default upper limit of 4000.

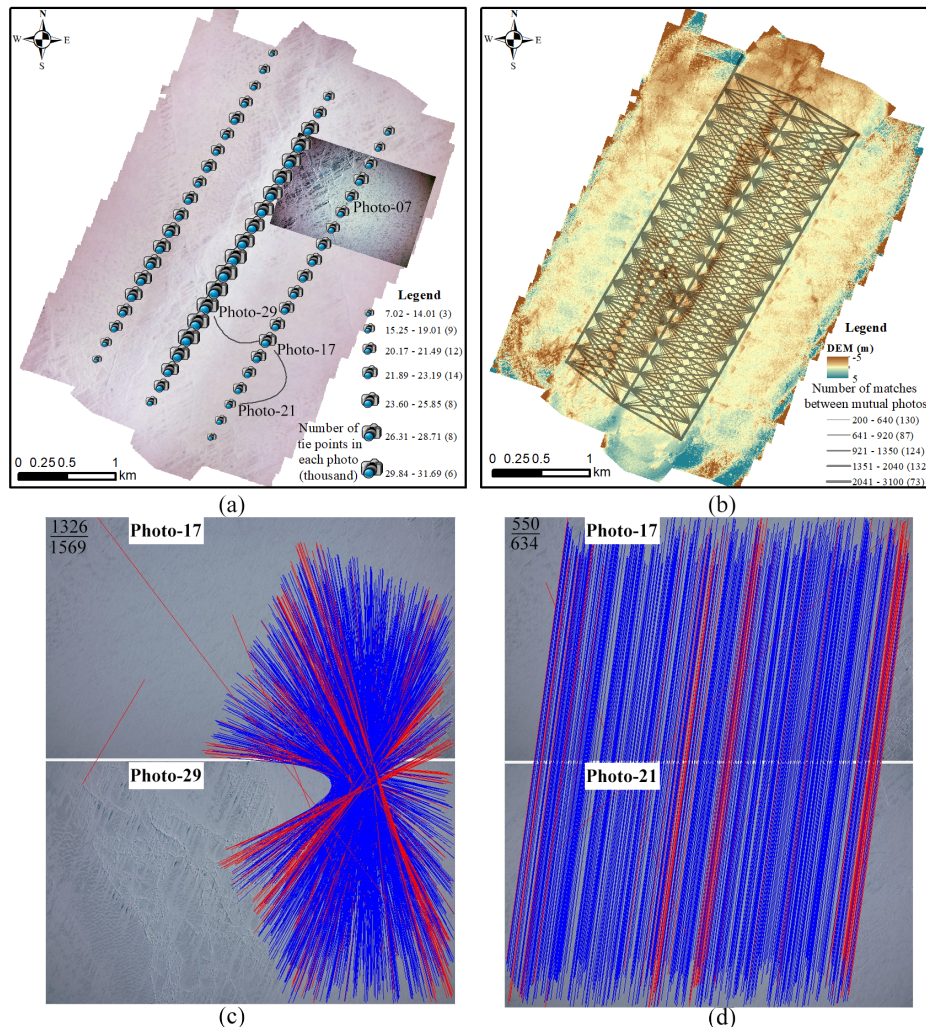


Figure 5. The matching results after alignment optimization. Sortie-3 is shown here, as the example: (a) The coordinates of each exposure station, with the size of the camera representing the amount of tie-points in each photo. The number after each item in the legend denotes the counts falling into the corresponding category. The geo-rectified photo-07, whose discernible 'vignetting effect' cannot be neglected in image stitching, is overlaid on top of the orthomosaic. Two curves link photo-29 and photo-21 with photo-17, whose matching performances are shown in panels (c) and (d); (b) Alignment performance between each possible pair link among all 60 input photos, with the line thickness representing the amount of successful tie-points matches; (c) Matching result between photo-17 and photo-29, as an example of sideways-neighbouring areas. A total of 1326 out of the 1569 feature points were tied properly (blue links). The matching links are reversed due to the 180° difference of heading between adjacent courses. Red links denote local erroneous matches, which may severely deviate from the holistic pattern, which is dealt with in later camera orientation and sparse point cloud generation. (d) Matching result between photo-17 and photo-21, as an example of forward-neighbouring areas. A total of 550 out of the 634 feature points were tied properly. The nearest two neighbours were not selected here for visually clear purposes, since tie-point links are too dense to represent. The same symbology as in (c) is used.

Histograms of all three sorties are summarized in Figure 6. Sortie-1 obtained a similar distribution shape as sortie-3; the median is only slightly lower (21,699 versus 22,393); which is surprising, given the relatively low solar inclination at the time of sortie-1. Interestingly, sortie-2 performed poorly, in terms of relative optimal illumination; the high exposure of the orthomosaic may be directly linked to the lower number of tie-points retrieved from these images. The bright tone of the orthomosaic suggests that over-exposure may be the culprit. Again, in Figure 6h, there was no palpable difference between sortie-1 and sortie-3, but sortie-2 seems to be the strongest among the three. In essence, it is an underlying mirage, resulting from the single strip; this kind of unfavourable geometry forms no closed loop. According to the least-square theory in classic surveying, error can accumulate monotonically with no effective control.

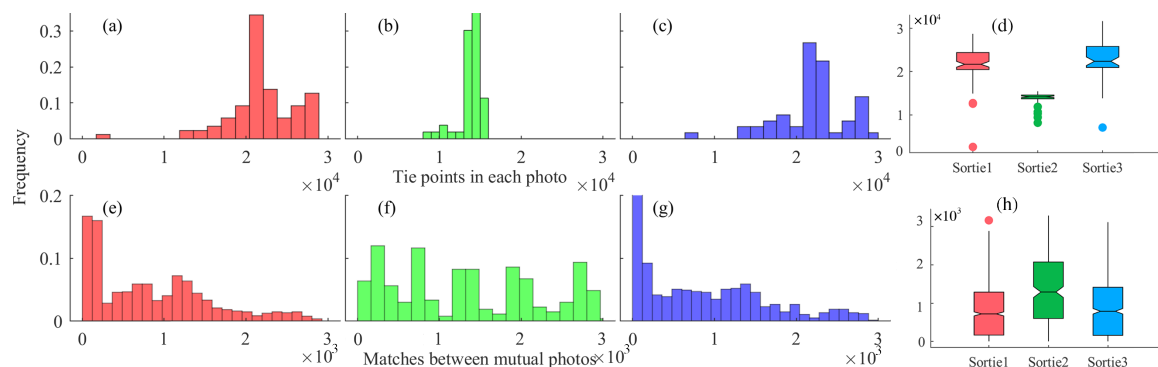


Figure 6. The histogram of tie-points quantity distribution in each photo from the three sorties: (a) Sortie-1, (b) sortie-2, and (c) sortie-3, (d) The notched box plot of the previous variable in the three sorties. The histogram of match quantity distribution in mutual photo pairs from the three sorties: (e) Sortie-1, (f) sortie-2, and (g) sortie-3, (h) The notched box plot of the previous variable in the three sorties. Note that the scale of the horizontal axis in the histogram plot is the same as that of vertical axis in the box plot in each row.

4.2. Exterior Orientation

In bundle block adjustment, errors from image matching and instrument measurement are appropriately allocated. In light of robust optimization, a large residual should arise if outliers were interposed a priori. Here, we explore sortie-1 adjustments after exterior orientation. To make units consistent, longitude and latitude are projected into planimetric coordinates, in metres.

The mean of the X , Y , and Z residual error components converge to zero, but this masks significant complexity. The residuals of the X and Y coordinates evolve synchronously, but the amplitude is larger for Y (see Figure 7a). Both experience saltation when shifting to the next strip at photo-31 and photo-62 (POS record), whilst the superimposed oscillations may reflect the effects of wind turbulence. However, most of the positional errors are introduced by the Z residuals, which experiences a residual error amplitude of >6 m along a single strip. We speculate that the dips of X and Y dimension in photo-62 could presumably be attributed to a gust of crosswind, which happened when the UAS was swerving to next strip.

A similar pattern appears for the orientation residuals (Figure 7b), but with mean bias offsets, which are positive for roll, yet negative for yaw and pitch. The most mysterious pattern occurs in yaw angle. Not only is the variation magnitude (left Y -axis) almost one order larger than that of pitch and roll (right Y axis), but also it oscillates back and forth coarsely. The same thing also happens in the other two sorties in Figure 8d; thus, we speculate the IMU might lose its fixation in the yaw dimension (see Section 5 for more discussion). Alternatively, this could reflect the wind's influence—if the wind was coming from a constant direction during sortie-1, it would cause the yaw to be offset one way when the drone was flying north (for example), and the opposite way when the drone was flying south.

Overall, it can be safely inferred that the Z and yaw measurements in the POS records are not reliable and, therefore, contribute the most to error adjustment.

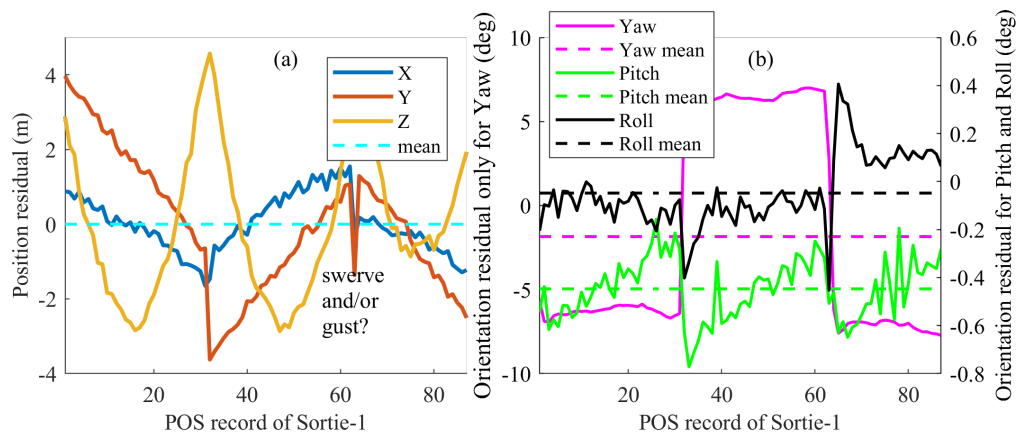


Figure 7. The position and orientation system (POS) residuals after alignment optimization. Sortie-1 is selected here as an example; for the residual distributions of all three sorties, please refer to Figure 8 for their distributions. (a) The positional residuals in the photo acquisition sequence. Note that the error accumulates quickly along the same strip, in particular for the Z dimension, which oscillates periodically. (b) The orientational residuals in photo acquisition sequence. Note the error of the yaw (left Y-axis) is an order larger than that of pitch and roll (right Y-axis), and the fluctuation amplitude of yaw is much larger as well. In contrast to the mean of positional residual converging to zero, the means of orientational residual are more or less biased.

The residual distribution from all three sorties are summarized in Table 2 and Figure 8. Except for yaw, the remaining five residual error components show a centralized, normal-like distribution, which corroborates the hypothesis in a later Monte-Carlo simulation [36]. Reasonably, the standard deviation of the yaw has to be excluded, as the input for next step’s evaluation.

Table 2. Standard Deviation Statistics Summary of the POS Residuals.

Mission No.	Position (m)			Orientation (deg)		
	X	Y	Z	Yaw	Pitch	Roll
sortie-1	0.7615	1.8153	1.9873	6.3752	0.1289	0.1443
sortie-2	3.1225	1.5849	0.7524	3.6204	0.0765	0.4688
sortie-3	1.4837	0.2925	0.5205	4.9438	0.2006	0.4193
mean		1.3689			0.2397 *	

* Stds of Yaw were excluded from calculation.

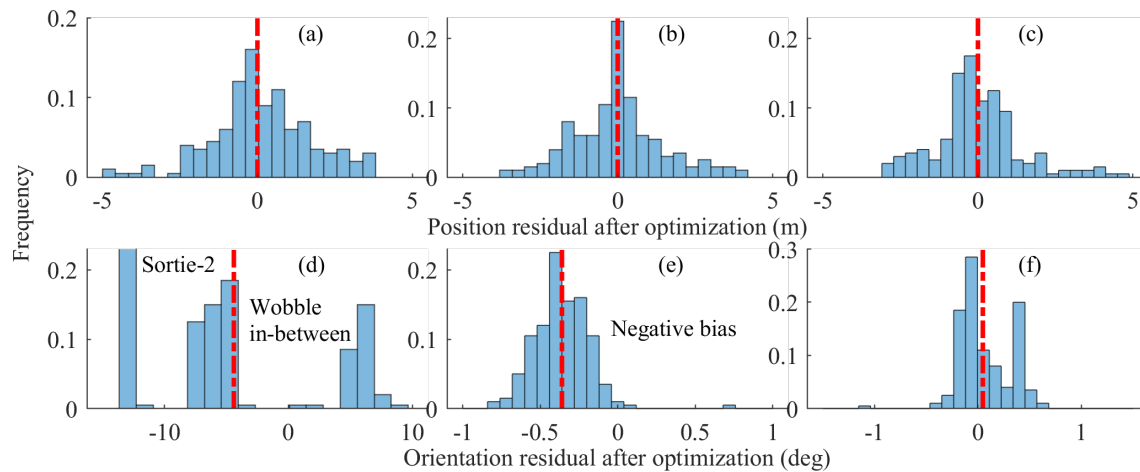


Figure 8. The POS residual histograms of all 200 photos from the three sorties after alignment optimization in Agisoft® PhotoScan, through which sparse cloud points were produced. (a–c) are for the positional records, X, Y, and Z, respectively, whose bell-shaped distributions are zero-centred (similar to Gaussian forms). The (d–f) are for the orientational records, yaw, pitch, and roll, respectively, whose distributions are much more complicated than that of the positional records.

4.3. Precision Evaluation

For the Monte Carlo precision analysis, the mean positional and orientation residual errors of 1.367 m and 0.24° (Table 2) were specified as the measurement accuracy of camera position and orientation. Bundle adjustments, forced by pseudo-random additions, were repeatedly executed in a form of sensitivity analysis, which allowed us to assess the effects of camera model parameter adjustment on the model precision.

The results of our precision analysis are displayed visually in Figure 9, and graphically in Figure 10. Figure 9 shows a numerically parallel distribution (i.e., decreasing precision with increasing distance from the centre of each sortie), but the orientation of this pattern of error propagation varies; these error ‘domes’ were elongated broadly north-south for X and west-east for Y. For X and Y, the precision errors ranged from a minimum of 0.15 m at the distortion centres, where both forward and side image overlaps were at their greatest, to >0.35 m at the survey periphery, where side image overlap is non-existent for the outermost images. A similar effect is observed for the Z component of the error, although with a slightly less pronounced precisional dome effect. Sortie-3, for which we retrieved the maximum number of key-points and tie-points (Figure 6d,h), constrained the Z precision to less than 0.5 m. Though sortie-1 achieved similar metrics in Section 4.1, the low solar altitude exerted real effects here. It is implied that the success rate of matching should be obviously less than 85% of sortie-3 (Figure 5c,d), where rough ridges abound.

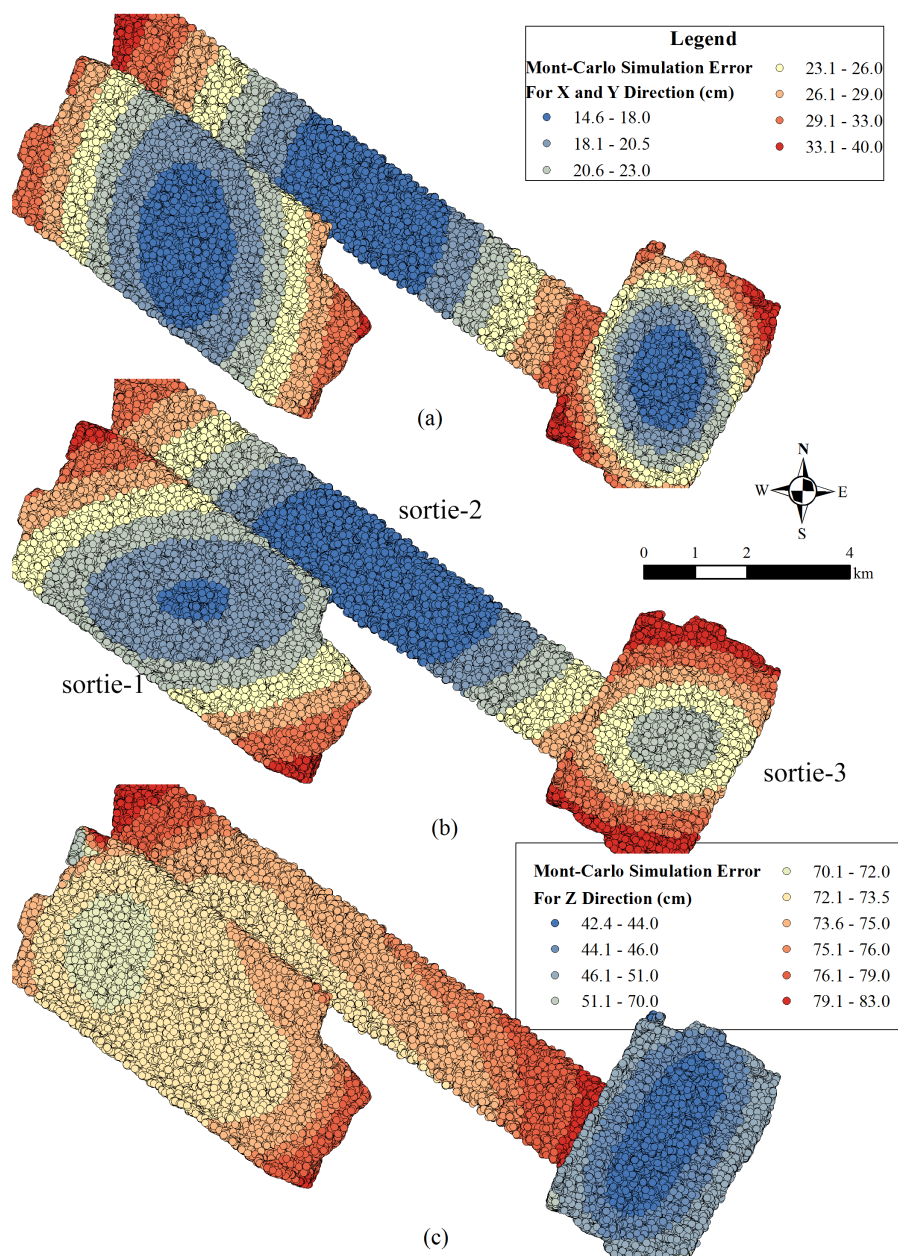


Figure 9. The 3D precision map of sparse point clouds through alignment optimization in Agisoft® PhotoScan, based on Monte Carlo simulations: (a) X, (b) Y, and (c) Z dimensions. The standard deviation of perturbation added into the original POS records is 1.37 m for GPS position and 0.24° for IMU orientation, as summarized in Table 2. The colour ramps for (a) and (b) are identical, whereas (c) possesses its own. Please refer to James et al. [36] for technical details of evaluation algorithm.

Taking sortie-1 as an example, once more, we explore the relationship of two kinds of errors induced from different sources. The total precision Y is slightly larger than that of X, but much smaller than that of Z, revealing the same pattern as the positional residuals in Figure 7a. For shape-only error, the vertical uncertainty is an order of magnitude greater than that of X or Y. We expect this finding, as planimetric coordinates were directly retrieved from the two-dimensional photograph but depth information was estimated from the redundant parallax observation. From Figure 10g–i, we confirm that the accuracy of the final photogrammetric products was mainly limited by weak georeferencing, based on the fact that shape-only errors only accounted for about 5% planimetrically or 20% vertically, in total.

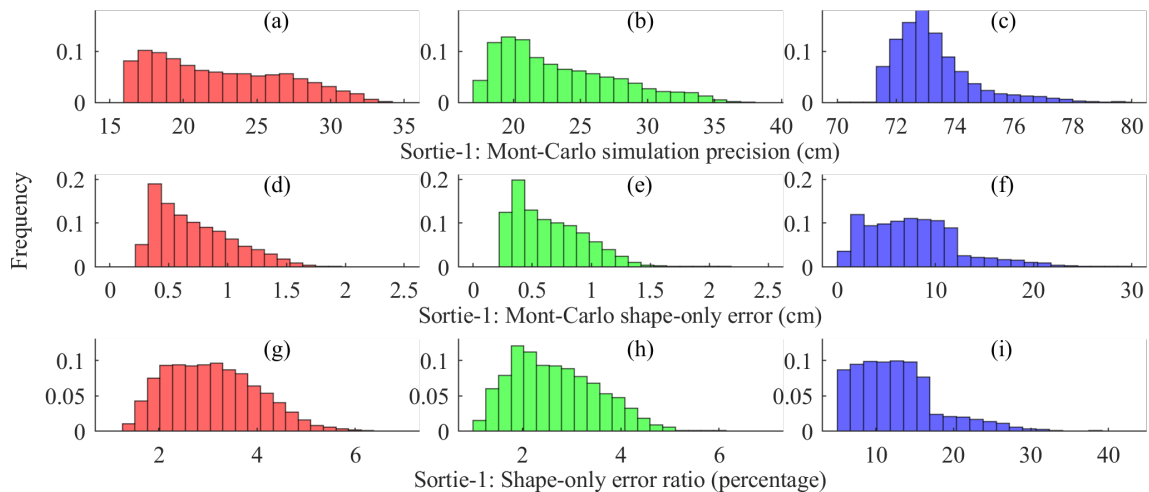


Figure 10. The 3D precision histogram of the sparse point cloud, based on Monte Carlo simulation. Sortie-1 was selected as an example. For spatial variability of all three sorties' 3D precision, please refer to Figure 9. The first row, (a–c), are for whole precision from the Monte Carlo simulation; The second row, (d–f), are for shape-only errors, regardless of the exterior POS record or ground control. The third row, (g–i), are for the proportions of shape-only error, accounting for all precision. The first, second, and third columns are for the X, Y, and Z dimension, respectively.

4.4. Surface Morphological Features

Shaped by the interplay of environmental forcing and internal stress, we observe a variety of morphological features on the sea ice surface. These features affect air-ice-ocean energy interactions, as well as posing risks for operational practices. The high-definition orthomosaic and elevation models are useful for characterizing sea ice morphology, since, when analyzed in conjunction with one another, it is possible to unveil fine-grain detail and relief variation on the ice surface. In this section, we identify and discuss a couple of morphological sea ice structures using our data.

Figure 11a,d are close-ups of the R/V Xuelong, which broke through the fast ice, as far as 847 m. Cargo containers were being unloaded on the ice surface, off the portside. The orthomosaic proved to be measurable by validating the vessel length from the image. The 167 m line-segment in (a) agrees surprisingly well with the actual measurement (167 m), especially given that this area lies at the end of a survey course. Even with ground control, large distortion in such an edge is inevitable, such as the asymmetric bias between two sides of the vessel.

Further offshore, Figure 11b,e show drift ice, moved by winds and currents, formed at the dynamic outer boundary of the landfast ice. Break-up behaviours associated with the brittle properties of ice were observed, which is an intrinsic response of solids to a strong external forcing. The locations of the artefacts highlighted in Figure 11d,e were anticipated, and are associated with spurious matches on water surface. Across the sea ice, we observe no obvious shear structures, probably because lateral collision did not take place under the persistent offshore winds and quick processes.

We highlight two parallel, curvilinear ridges in Figure 11g,i. When strong winds blow over, landfast ice (in its infant stage) forms cracks along fractures. The two individual blocks then advect divergently, before being weakly sutured together by a layer of newly-formed and thinner transitional ice. Noticeable texture of decaying, such as melt ponds scattered on the surface or dirty ice in the midst of bright white ice, could be a consequence of water flooding or brine seepage.

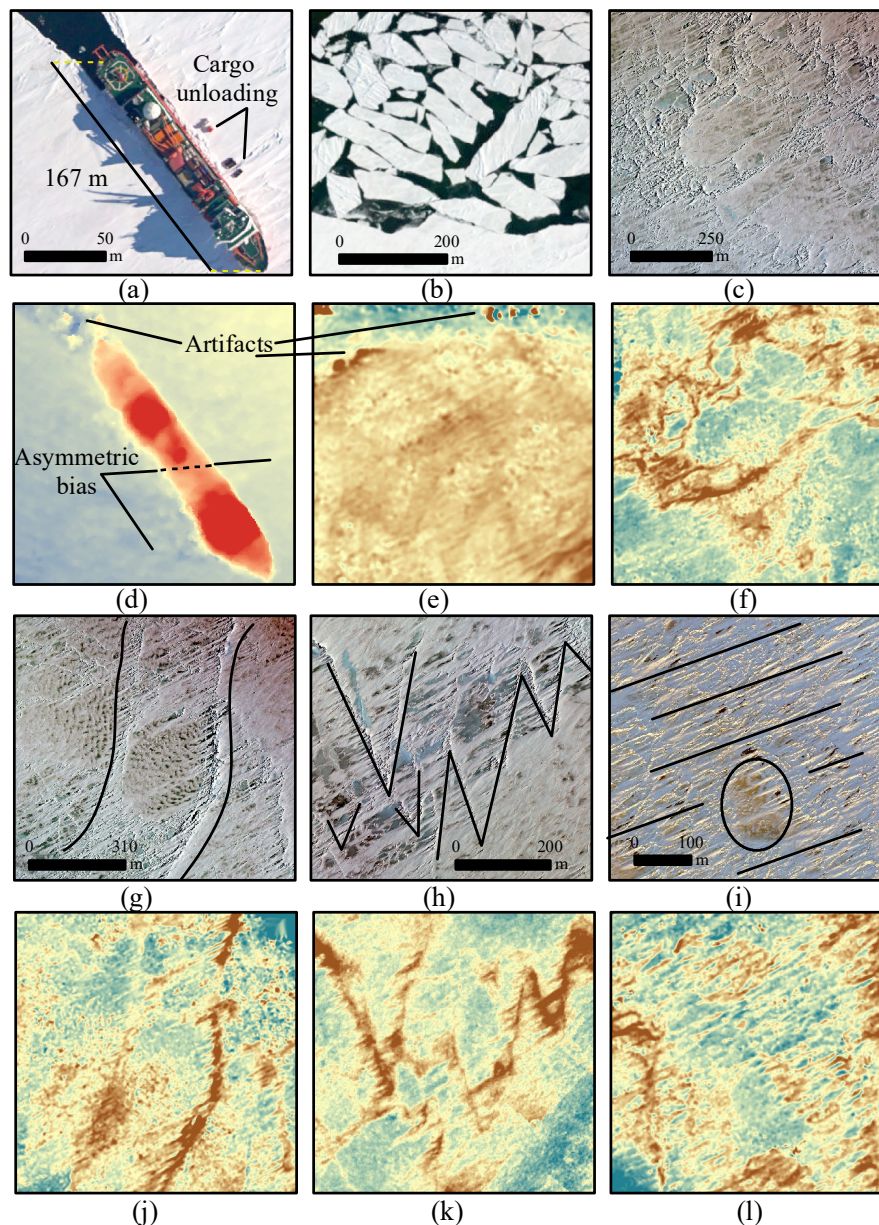


Figure 11. The typical surface geometric features selected from the orthomosaics and their corresponding local surface topography: (a) The anchored R/V Xuelong, with cargo unloading nearby. (b) Newly-broken chunks of ice floes close to the outer boundary of the landfast ice (lower part). (c) Extremely rough margin close to the outer boundary of the landfast ice (upper part). (d–f) are their upper panels’ corresponding surface elevation. Please note the unbalanced bias acting between the two flanks of the R/V Xuelong in (d), and little artifacts in the area of sea water in (e). (g) Two almost parallel and smoothly curved ice ridges, with melting pond-like features interspersed nearby. (h) Ice ridges in an opposing zigzagged shape. (i) Densely distributed and nearly parallel snow dunes with a flat ice floe inside. (j–l) are their upper panels’ corresponding surface elevation. Note that all the orthomosaic and surface elevation images are locally stretched to enhance the visualization. Please refer to boxes in Figure 4 for all panel’s geographic extent.

In Figure 11h,k, we observe a phenomenon known as ‘finger rafting’, whereby, as the name suggests, two sheets collide and interlock into each other to form intertwined edges. If the impingement continues, the ridge height can become exaggerated. The sail above the waterline reaches up to 5 m, which implies that the keel below the waterline should be at least four times thicker. Through such

mechanisms, fast ice contributes proportionally more volume by area than other types of Antarctic sea ice [5].

In Figure 11i,j, we observe the redistribution of surface snow by strong winds to form sastrugi-like forms, or wind ripples. From a photogrammetric perspective, these hard-packed snow dunes roughen the ice surface and provide vertical feature expression, which help to facilitate depth-matching, by virtue of their vertical surface expression. We also notice the lower elevation inside the annotated ellipse (Figure 11i); we attribute this to pan ice formation, which has thereafter been incorporated into the landfast sheet through advection [44].

In terms of satellite SAR and microwave altimeter, the peculiar geometry in (g), (h), and (i) would cause anisotropic observation (intensity or waveform). If such structures extended to a larger spatial scale, it can be expected that samples from ascending and descending orbits would vary significantly.

5. Discussions

Our direct georeferencing approach has obvious logistical benefits for UAS surveys over hazardous areas, including Antarctic sea ice; however, this study has also revealed notable operational considerations for UAS deployment in cold environments, as well as precisional deficiencies, which we discuss below.

5.1. Hardware and Operation

The two previous UAS surveys conducted in this field both employed rotary wing-type UAS. This technology is adaptable but is limited by battery endurance; most systems of this type are only capable of flight times of <15 min in cold environments [25,26]. To maximize battery life, we warmed our batteries to at least 5 °C pre-flight, which had a noticeable effect on flight time.

Due to climatic extremes, UAS operations at high latitudes are heavily weather-dependent. During the Antarctic austral summer, strong winds and thick fogs are common, and the short windows of fair weather must be taken full advantage. Further, knowledge of the locality and up-to-date meteorology is key; strong turbulence in the upper atmosphere should also be taken into consideration, and we recommend that UAS operators also review high-altitude meteorological reports prior to UAS deployment. We also demonstrate the utility of near-real-time satellite imagery for informing study site identification and mission planning [45]; in this study, the availability of high-resolution Sentinel 2 imagery was invaluable for this purpose, and we advocate pre-flight acquisition and scrutiny of satellite remote sensing data products to inform low-altitude UAS sorties.

The exceptional background, not encountered outside Antarctica, is the polar daytime in high latitudes; whereas it is widely acknowledged that sub-optimal illumination can be detrimental to photogrammetric processing [42]. We find that, across a relatively subdued topography, the low solar altitude at austral summer dawn and dusk reveals fine-grained topographic relief through the casting of exaggerated shadows. Counter-intuitively, these shadows appear to aid photogrammetric reconstruction in this setting. Thus, at extreme latitudes, there therefore exists an operational trade-off between ensuring sufficient radiance intensity (in favour of optimal illumination) and a low solar angle (in favour of highlighting small-scale surface features). On the other hand, the strong illumination at noon might result in over-exposure for high-albedo surfaces and ought to be avoided; which contrasts the usual recommendations to undertake UAS surveys during periods of maximum solar illumination [42].

5.2. Processing and Precision

Typically, the minimum standard for quality evaluation of SfM-MVS-derived data products comprises the statement of root mean square error (RMSE) values when compared to some ground truth measurements [31,46]. However, such simple metrics cannot provide a full description of the uncertainty associated with SfM photogrammetry [47,48], and even low mean error values can mask large variations and a significant intricacy in the error signal. We therefore exploit tools for assessing

the SfM-MVS model quality through an in-depth precisional analysis. These data offer us a chance to investigate network strength along individual and multiple parallel flight lines.

In the absence of a dense network of survey-grade ground controls, the best-fit seven parameters affine (three translation, three rotation, and one scale) rigid-body Helmert transform depends entirely on extrinsic measurements. Accordingly, errors in the on-board GPS record propagate through into the final photogrammetric solution [48,49]. For our Polar Hawk-III, precise, directly-georeferenced work is restricted by low-quality measurements of vehicle height (multi-metre) and yaw angle ($3^\circ \sim 6^\circ$), perhaps from a loosening IMU. Later IMU data checks revealed that yaw angles should demonstrate a similar magnitude of error as roll and pitch ($<0.5^\circ$), and so we attribute the large step-changes in our IMU precisional error signal (Figure 7b) to insecure IMU fixture and the failure of pre-flight checks to pick this up, combined with craft shaking during directional change at the end of each image strip (which could serve to move the IMU unit).

To systematically explore photogrammetric and direct georeferencing uncertainty, a POS perturbation method, based on Monte Carlo simulation, was employed. According to the empirical rule, proposed by Carbonneau and Dietrich [48], 1:1000 could be regarded as the inherent limit to SfM precision level. Our topographic data can be rated into the ‘good quality’ category as the precision of the sparse cloud in all dimensions never exceeds 1500 m:1000. In the sense of image sampling configuration, the simulated planimetric uncertainty is about the same as the GSD (20 cm), and two to four times higher in the vertical dimension. Similar proportional relationships have also been found in previous studies [27,50].

As a further check of the accuracy of our data, we employed simple trigonometry. At the centre of sortie-1 we discovered an ingested iceberg (see Figure 12). By comparing the tangent of height and shadow length, and sun geometry, we find they are consistent with each other as well, exhibiting a degree of topographic consistency in our data products, which are otherwise characterized by systematic topographic inconsistency and artefacts (Figure 4).

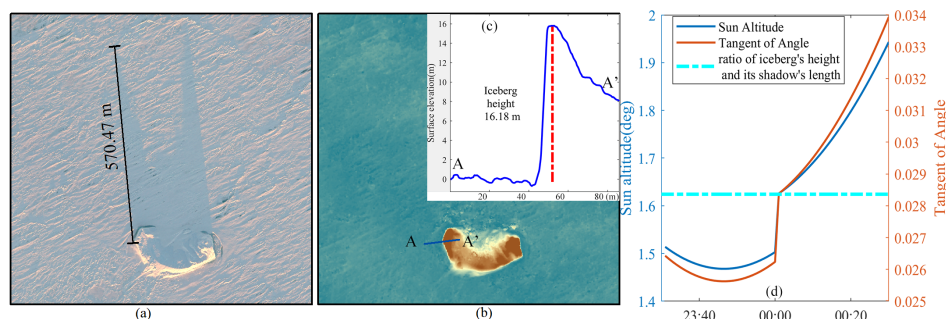


Figure 12. An iceberg was entrapped in landfast sea ice in sortie-1. (a) Orthomosaic imagery of the iceberg and its elongated shadow (570.47 m). (b) Surface elevation model of the iceberg and surrounding smooth sea ice. (c) The elevation profile of the blue line in (b), with a height of 16.18 m. (d) The evolution of solar altitude angle and its tangent ratio during the sortie-1 operation in polar day, and ratio of iceberg’s height and its shadow’s length. Note the leap of solar altitude before and after midnight, as a result of the discretization artefact in the approximation algorithm.

Establishing a well-distributed GCP network (including redundancy), is time-consuming, costly, and, depending on the setting, can be logistically difficult or hazardous [51]. Drawing on our experience and published recommendations, we indicate some directions worth the resource and effort in improving the quality of direct georeferencing-derived UAV-SfM data products. Network geometry can be further reinforced by including (1) oblique imagery from convergence observations; (2) photo acquisition from multiple heights; (3) additional cross-strips; (4) increasing image overlap, or even simply the number of images; (5) a well-defined camera distortion model; and (6) extra radial detrend correction [31,36,48,49]. Further, in the case where fresh snow dominates the ice surface, which reflects nearly 100% of the incoming solar radiation in the visible part of electromagnetic spectrum

($\lambda = 0.37\sim 0.7\mu\text{m}$), additional near-infrared band information ($\lambda = 0.7\sim 0.85\mu\text{m}$), combined with pre-processing steps to enhance image texture before matching [42] could be used to supplement the optical information [27] for photogrammetric reconstruction. Finally, Gindraux et al. [30] argued that snow weathering can significantly affect reconstruction success; one-day-old snow is inherently more texturally complex than fresh snow, an effect which magnifies with prolonged persistent weathering by katabatic winds.

5.3. Potential UAV-SfM Applications on Sea Ice

UAS-SfM-derived data products provide opportunities to scrutinize fast ice surface features in unparalleled detail (Figure 11). Such information could be of interest to various applications, including characterization of the size and spacing distributions of pressure ridges [52], surface roughness estimation [53,54], melt pond identification and extraction [55,56], icebreaker navigation [38], exploration- or transportation-planning over ice based on deformation structures [57,58], and even free-drift iceberg tagging [59].

If time-series data were collected, SfM-MVS data products, combined with DSM differencing methods, could be used to quantify the dynamical behaviours of sea ice decay in unprecedented spatial and temporal resolutions. Taking this further, colour thresholding, derived from the colour distribution histograms of the images, could be used to identify and track melt pond expansion, permitting estimation of the surface heat budget between the ice and atmosphere during sea ice decay [60]. Correlation-based image tracking techniques have already showed satisfactory outcomes in sea ice displacement retrieval from ENVISAT data [61], and similar approaches could be applied to time series of UAV-SfM orthomosaics to track small-scale motion and deformations, provided the UAS orthomosaics are accurately georeferenced [62]. The derivative of strain rates is a fundamental factor in multi-temporal sea ice stability research [34], and is a scale-dependent variable which cannot be linearly extrapolated from coarse-scale space observation [7].

Approaches to geophysical measurement are dictated by the spatio-temporal scales of the phenomenon of interest, as they relate to the scientific question(s), and technical feasibility [40]. Regarding possible future applications of our method in sea ice settings, it might be possible, for example, to extract the freeboard of boundary ice floes [63] and, in turn, derive ice thickness by substituting these data into hydrostatic equations. As has already been demonstrated in an ice sheet setting [45], the linear combination of weighted RGB raw brightness could serve as a proxy for surface albedo, which is a parameter of great importance in remote sensing and energy balance applications for sea ice [33]; UAV-derived albedo data may prove useful for validating estimations of albedo from spaceborne sensors [45]. Similarly, the use of multi- and hyper-spectral sensors could help to develop a spectral library for different kinds of snow and sea ice facies [18]. From a field logistics and planning perspective, data such as ours could be used to identify areas prone to fracture or severe deformation and inform on-ice field activities.

Some of the applications described above require topographic data products with sub-decimetre accuracies, which our results do not fulfill. However, the technology already exists which can do so: GNSS-supported aerial triangulation methods have demonstrated the capacity to achieve survey decimetric precisions for piloted UAV-SfM surveys, using differential GPS synchronized with image capture [36,64,65]. Meanwhile, some tests carried out achieved a centimetric accuracy, which rivals that typically achievable using traditional GCP-supported orientation [32,51]. Whilst we lacked the ability to differentially correct our on-board GPS data for the present study, this method holds promise for sea ice survey applications.

6. Conclusions and Outlook

Here, we have presented the first UAV-SfM study of landfast Antarctic sea ice. Mapping landfast sea ice efficiently and accurately at high spatial resolution is a non-trivial task. In this, and other environments, UAS-SfM-derived data products sit at an intermediate observational level, between

spaceborne remote sensing and ground-based sampling, and represent a more cost-effective alternative to manned aerial observation. The highly-automated and relatively accessible SfM workflow reduces the technical knowledge barriers typically required for rigorous photogrammetry.

Counter-intuitively, we find that low solar illumination angles promote the enhancement of surface texture through shadows cast on the fast ice, which promotes key-point identification and tie-point matching of sufficient volume to enable geometric network reconstruction. Through the analysis of exterior orientation residuals, the vehicle height and yaw angle emerge to be the most significant sources of precision error, whilst the relative shape of the topography derived within the internal network is good (<1.5 cm for X/Y and 10 cm for Z), but its overall georeferencing performance is weakly constrained, due to the quality of our on-board POS records (~20 cm for X/Y and 70 cm for Z). Monte Carlo-based analysis of the survey precision sheds light on the spatial distribution of the survey error, and can inform mitigative measures to combat the introduction of model deformations.

Our data permit a meaningful interpretation of fine-scale sea ice morphology and provide a starting point for more in-depth analysis and scientific applications, such as surface roughness estimation, and also support practical and logistical decision-making. We anticipate that low-cost and on-demand UAS surveying will become a routine tool for polar expeditionary science.

Supplementary Materials: Data Accessibility: The analysis data and processing codes for this study, including some supplementary figures not shown in text, have been made publicly available at the author's GitHub repository: <https://github.com/bwbj/PhotoScanResultAssessment> under MIT license.

Author Contributions: T.L. processed and analyzed the data, and wrote the manuscript; B.Z. and C.M. designed the experiments and collected data; Z.L. and M.J.W. discussed the results, and edited the text; M.S., F.H., Y.L., Z.C., M.Z., and X.L. investigated the results; X.C. investigated the results, revised the manuscript, and supervised this study.

Funding: This work was supported by the National key research and development Program of China (No. 2018YFA0605403), National Natural Science Foundation of China (Grant No. 41830536, 41676176 and 41676182); the Chinese Polar Environment Comprehensive Investigation and Assessment Program; Qian Xuesen Lab.-DFH Sat. Co. Joint Research and Development Fund; and the Fundamental Research Funds for the Central Universities in China. This work was also supported by the UK NERC, through the Centre for the Observation and Modelling of Earthquakes, Volcanoes, and Tectonics (COMET, ref.: come30001) and by the European Space Agency through the ESA-MOST DRAGON-4 project (ref. 32244).

Acknowledgments: We greatly thank ESA for providing the Sentinel-2 high resolution optical satellite remote sensing imagery (<https://scihub.copernicus.eu/>), and BAS for providing the BedMap2 DEM (<https://www.bas.ac.uk/project/bedmap-2/>). We want to thank Mr. Pasumansky from Agisoft forum for sharing python codes (<http://www.Agisoft.com/forum/index.php?topic=6989>) and James from Lancaster University for releasing the innovative SfM-GeoRef software (http://www.lancaster.ac.uk/staff/jamesm/software/sfm_georef.htm). Gratitude ought to be expressed to all members participating in 33th and 34th CHINARE for their valuable field support, both physically and morally. We, finally, would like to extend sincere appreciation to Shijie Zhang and other helpful engineers in Feima Robotics laboratory. The comments from Prof. Hilmar Gudmundsson and anonymous reviewers substantively improved the original manuscript.

Conflicts of Interest: The authors declare no conflict of interest.

Abbreviations

The following abbreviations are used in this manuscript:

AAD	Australia Antarctic Division
AFIN	Antarctic Fast-Ice Network
API	Application Program Interface
BAS	British Antarctic Survey
CFCs	Carbon Fiber Composites
CHINARE	Chinese National Antarctic Scientific Research Expedition
DSM	Digital Surface Model
EPSCG	European Petroleum Survey Group
ESA	European Space Agency
GCP	Ground Control Point
GNSS	Global Navigation Satellite System

GSD	Ground Sampling Distance
IFOV	Instantaneous Field Of View
IMU	Inertial Measurement Unit
LiDAR	Light Detection And Ranging
LIMA	Landsat Image Mosaic of Antarctica
POS	Position and Orientation System
MVS	Multi-View Stereopsis
RGB	Red-Green-Blue
RMSE	Root Mean Square Error
RTK	Real Time Kinetic
SfM	Structure from Motion
UAS	Unmanned Aerial System
USGS	United States Geological Survey
UTM	Universal Transverse Mercator coordinate system
WGS84	World Geodetic System 1984

References

1. Marbouti, M.; Praks, J.; Antropov, O.; Rinne, E.; Leppäranta, M. A Study of Landfast Ice with Sentinel-1 Repeat-Pass Interferometry over the Baltic Sea. *Remote Sens.* **2017**, *9*, 833, doi:10.3390/rs9080833. [[CrossRef](#)]
2. Fraser, A.D.; Massom, R.A.; Michael, K.J. Generation of high-resolution East Antarctic landfast sea-ice maps from cloud-free MODIS satellite composite imagery. *Remote Sens. Environ.* **2010**, *114*, 2888–2896, doi:10.1016/j.rse.2010.07.006. [[CrossRef](#)]
3. Heil, P.; Allison, I.; Lytle, V.I. Seasonal and interannual variations of the oceanic heat flux under a landfast Antarctic sea ice cover. *J. Geophys. Res. Ocean.* **1996**, *101*, 25741–25752, doi:10.1029/96jc01921. [[CrossRef](#)]
4. Massom, R.; Hill, K.; Barbraud, C.; Adams, N.; Ancel, A.; Emmerson, L.; Pook, M. Fast ice distribution in Adélie Land, East Antarctica: interannual variability and implications for emperor penguins *Aptenodytes forsteri*. *Mar. Ecol. Prog. Ser.* **2009**, *374*, 243–257, doi:10.3354/meps07734. [[CrossRef](#)]
5. Giles, A.B.; Massom, R.A.; Lytle, V.I. Fast-ice distribution in East Antarctica during 1997 and 1999 determined using RADARSAT data. *J. Geophys. Res.* **2008**, *113*, doi:10.1029/2007jc004139. [[CrossRef](#)]
6. Dammann, D.O.; Eicken, H.; Meyer, F.J.; Mahoney, A.R. Assessing small-scale deformation and stability of landfast sea ice on seasonal timescales through L-band SAR interferometry and inverse modeling. *Remote Sens. Environ.* **2016**, *187*, 492–504, doi:10.1016/j.rse.2016.10.032. [[CrossRef](#)]
7. Spreen, G.; Kwok, R.; Menemenlis, D.; Nguyen, A.T. Sea-ice deformation in a coupled ocean–sea-ice model and in satellite remote sensing data. *Cryosphere* **2017**, *11*, 1553–1573, doi:10.5194/tc-11-1553-2017. [[CrossRef](#)]
8. Lu, P.; Li, Z.; Cheng, B.; Lei, R.; Zhang, R. Sea ice surface features in Arctic summer 2008: Aerial observations. *Remote Sens. Environ.* **2010**, *114*, 693–699, doi:10.1016/j.rse.2009.11.009. [[CrossRef](#)]
9. Wright, N.C.; Polashenski, C.M. Open-source algorithm for detecting sea ice surface features in high-resolution optical imagery. *Cryosphere* **2018**, *12*, 1307–1329, doi:10.5194/tc-12-1307-2018. [[CrossRef](#)]
10. Landy, J.C.; Komarov, A.S.; Barber, D.G. Numerical and Experimental Evaluation of Terrestrial LiDAR for Parameterizing Centimeter-Scale Sea Ice Surface Roughness. *IEEE Trans. Geosci. Remote Sens.* **2015**, *53*, 4887–4898, doi:10.1109/tgrs.2015.2412034. [[CrossRef](#)]
11. Landy, J.C.; Isleifson, D.; Komarov, A.S.; Barber, D.G. Parameterization of Centimeter-Scale Sea Ice Surface Roughness Using Terrestrial LiDAR. *IEEE Trans. Geosci. Remote Sens.* **2015**, *53*, 1271–1286, doi:10.1109/tgrs.2014.2336833. [[CrossRef](#)]
12. James, M.R.; Robson, S. Straightforward reconstruction of 3D surfaces and topography with a camera: Accuracy and geoscience application. *J. Geophys. Res. Earth Surf.* **2012**, *117*, F03017, doi:10.1029/2011jf002289. [[CrossRef](#)]
13. Westoby, M.; Brasington, J.; Glasser, N.; Hambrey, M.; Reynolds, J. ‘Structure-from-Motion’ photogrammetry: A low-cost, effective tool for geoscience applications. *Geomorphology* **2012**, *179*, 300–314, doi:10.1016/j.geomorph.2012.08.021. [[CrossRef](#)]
14. Fonstad, M.A.; Dietrich, J.T.; Courville, B.C.; Jensen, J.L.; Carbonneau, P.E. Topographic structure from motion: A new development in photogrammetric measurement. *Earth Surf. Process. Landf.* **2013**, *38*, 421–430. doi:10.1002/esp.3366. [[CrossRef](#)]

15. Colomina, I.; Molina, P. Unmanned aerial systems for photogrammetry and remote sensing: A review. *ISPRS J. Photogramm. Remote Sens.* **2014**, *92*, 79–97, doi:10.1016/j.isprsjprs.2014.02.013. [[CrossRef](#)]
16. Pajares, G. Overview and Current Status of Remote Sensing Applications Based on Unmanned Aerial Vehicles (UAVs). *Photogramm. Eng. Remote Sens.* **2015**, *81*, 281–330, doi:10.14358/pers.81.4.281. [[CrossRef](#)]
17. Zmarz, A.; Rodzewicz, M.; Dąbski, M.; Karsznia, I.; Korczak-Abshire, M.; Chwedorzewska, K.J. Application of UAV BVLOS remote sensing data for multi-faceted analysis of Antarctic ecosystem. *Remote Sens. Environ.* **2018**, *217*, 375–388, doi:10.1016/j.rse.2018.08.031. [[CrossRef](#)]
18. Bhardwaj, A.; Sam, L.; Martín-Torres, F.J.; Kumar, R. UAVs as remote sensing platform in glaciology: Present applications and future prospects. *Remote Sens. Environ.* **2016**, *175*, 196–204, doi:10.1016/j.rse.2015.12.029. [[CrossRef](#)]
19. Dammann, D.O.; Eicken, H.; Mahoney, A.R.; Saitet, E.; Meyer, F.J.; George, J.C.C. Traversing Sea Ice - Linking Surface Roughness and Ice Trafficability Through SAR Polarimetry and Interferometry. *IEEE J. Sel. Top. Appl. Earth Obs. Remote Sens.* **2018**, *11*, 416–433, doi:10.1109/jstars.2017.2764961. [[CrossRef](#)]
20. Funaki, M.; Hirasawa, N. Outline of a small unmanned aerial vehicle (Ant-Plane) designed for Antarctic research. *Polar Sci.* **2008**, *2*, 129–142. doi:10.1016/j.polar.2008.05.002. [[CrossRef](#)]
21. Goetzendorf-Grabowski, T.; Rodzewicz, M. Design of UAV for photogrammetric mission in Antarctic area. *Proc. Inst. Mech. Eng. Part G J. Aerosp. Eng.* **2016**, *231*, 1660–1675, doi:10.1177/0954410016656881. [[CrossRef](#)]
22. Westoby, M.J.; Dunning, S.A.; Woodward, J.; Hein, A.S.; Marrero, S.M.; Winter, K.; Sugden, D.E. Sedimentological characterization of Antarctic moraines using UAVs and Structure-from-Motion photogrammetry. *J. Glaciol.* **2015**, *61*, 1088–1102, doi:10.3189/2015jog15j086. [[CrossRef](#)]
23. Leary, D. Drones on ice: An assessment of the legal implications of the use of unmanned aerial vehicles in scientific research and by the tourist industry in Antarctica. *Polar Rec.* **2017**, *53*, 343–357, doi:10.1017/s0032247417000262. [[CrossRef](#)]
24. Sanderson, K. Unmanned craft chart the Antarctic winter. *Nature* **2008**, doi:10.1038/news.2008.680. [[CrossRef](#)]
25. Williams, G.; Fraser, A.; Lucieer, A.; Turner, D.; Cougnon, E.; Kimball, P.; Toyota, T.; Maksym, T.; Singh, H.; Nitsche, F.; et al. Drones in a Cold Climate. *Eos* **2016**, *97*, doi:10.1029/2016eo043673. [[CrossRef](#)]
26. Division, A.A. Aurora Australis Uses Drone Technology to Navigate Sea Ice. 2015. Available online: <http://www.antarctica.gov.au/news/2015/aurora-australis-uses-drone-technology-to-navigate-sea-ice> (accessed on 20 January 2012)
27. Bühler, Y.; Adams, M.S.; Stoffel, A.; Boesch, R. Photogrammetric reconstruction of homogenous snow surfaces in alpine terrain applying near-infrared UAS imagery. *Int. J. Remote Sens.* **2017**, *38*, 3135–3158, doi:10.1080/01431161.2016.1275060. [[CrossRef](#)]
28. Wang, M.; Su, J.; Li, T.; Wang, X.; Ji, Q.; Cao, Y.; Lin, L.; Liu, Y. Determination of Arctic melt pond fraction and sea ice roughness from Unmanned Aerial Vehicle (UAV) imagery. *Adv. Polar Sci.* **2018**, *29*, 181–189.
29. Tonkin, T.; Midgley, N. Ground-Control Networks for Image Based Surface Reconstruction: An Investigation of Optimum Survey Designs Using UAV Derived Imagery and Structure-from-Motion Photogrammetry. *Remote Sens.* **2016**, *8*, 786, doi:10.3390/rs8090786. [[CrossRef](#)]
30. Gindraux, S.; Boesch, R.; Farinotti, D. Accuracy Assessment of Digital Surface Models from Unmanned Aerial Vehicles' Imagery on Glaciers. *Remote Sens.* **2017**, *9*, 186, doi:10.3390/rs9020186. [[CrossRef](#)]
31. Jaud, M.; Passot, S.; Allemand, P.; Dantec, N.L.; Grandjean, P.; Delacourt, C. Suggestions to Limit Geometric Distortions in the Reconstruction of Linear Coastal Landforms by SfM Photogrammetry with PhotoScan[®] and MicMac[®] for UAV Surveys with Restricted GCPs Pattern. *Drones* **2018**, *3*, 2, doi:10.3390/drones3010002. [[CrossRef](#)]
32. Benassi, F.; Dall'Asta, E.; Diotri, F.; Forlani, G.; di Cella, U.M.; Roncella, R.; Santise, M. Testing Accuracy and Repeatability of UAV Blocks Oriented with GNSS-Supported Aerial Triangulation. *Remote Sens.* **2017**, *9*, 172, doi:10.3390/rs9020172. [[CrossRef](#)]
33. Shokr, M.; Sinha, N. *Sea Ice*; John Wiley & Sons, Inc.: Hoboken, NJ, USA, 2015. doi:10.1002/9781119028000.
34. Dammann, D.O.; Eicken, H.; Mahoney, A.R.; Meyer, F.J.; Freymueller, J.T.; Kaufman, A.M. Evaluating landfast sea ice stress and fracture in support of operations on sea ice using SAR interferometry. *Cold Reg. Sci. Technol.* **2018**, *149*, 51–64, doi:10.1016/j.coldregions.2018.02.001. [[CrossRef](#)]

35. Dammann, D.O.; Eriksson, L.E.B.; Mahoney, A.R.; Eicken, H.; Meyer, F.J. Landfast sea ice stability–mapping pan-Arctic ice regimes with implications for ice use, subsea permafrost and marine habitats. *Cryosphere Discuss.* **2018**, 1–23, doi:10.5194/tc-2018-129. [[CrossRef](#)]
36. James, M.R.; Robson, S.; Smith, M.W. 3-D uncertainty-based topographic change detection with structure-from-motion photogrammetry: Precision maps for ground control and directly georeferenced surveys. *Earth Surf. Process. Landf.* **2017**, *42*, 1769–1788, doi:10.1002/esp.4125. [[CrossRef](#)]
37. Wang, X.; Cheng, X.; Hui, F.; Cheng, C.; Fok, H.; Liu, Y. Xuelong Navigation in Fast Ice Near the Zhongshan Station, Antarctica. *Mar. Technol. Soc. J.* **2014**, *48*, 84–91, doi:10.4031/mts.j.48.1.5. [[CrossRef](#)]
38. Hui, F.; Zhao, T.; Li, X.; Shokr, M.; Heil, P.; Zhao, J.; Zhang, L.; Cheng, X. Satellite-Based Sea Ice Navigation for Prydz Bay, East Antarctica. *Remote Sens.* **2017**, *9*, 518, doi:10.3390/rs9060518. [[CrossRef](#)]
39. Lei, R.; Li, Z.; Cheng, B.; Zhang, Z.; Heil, P. Annual cycle of landfast sea ice in Prydz Bay, east Antarctica. *J. Geophys. Res.* **2010**, *115*, doi:10.1029/2008jc005223. [[CrossRef](#)]
40. Heil, P.; Gerland, S.; Granskog, M.A. An Antarctic monitoring initiative for fast ice and comparison with the Arctic. *Cryosphere Discuss.* **2011**, *5*, 2437–2463, doi:10.5194/tcd-5-2437-2011. [[CrossRef](#)]
41. Pedersen, C.; Hall, R.; Gerland, S.; Sivertsen, A.; Svenøe, T.; Haas, C. Combined airborne profiling over Fram Strait sea ice: Fractional sea-ice types, albedo and thickness measurements. *Cold Reg. Sci. Technol.* **2009**, *55*, 23–32, doi:10.1016/j.coldregions.2008.08.004. [[CrossRef](#)]
42. Cimoli, E.; Marcer, M.; Vandecrux, B.; Bøggild, C.E.; Williams, G.; Simonsen, S.B. Application of Low-Cost UASs and Digital Photogrammetry for High-Resolution Snow Depth Mapping in the Arctic. *Remote Sens.* **2017**, *9*, 1144, doi:10.3390/rs9111144. [[CrossRef](#)]
43. Immerzeel, W.; Kraaijenbrink, P.; Shea, J.; Shrestha, A.; Pellicciotti, F.; Bierkens, M.; de Jong, S. High-resolution monitoring of Himalayan glacier dynamics using unmanned aerial vehicles. *Remote Sens. Environ.* **2014**, *150*, 93–103, doi:10.1016/j.rse.2014.04.025. [[CrossRef](#)]
44. Druckenmiller, M.L.; Eicken, H.; Johnson, M.A.; Pringle, D.J.; Williams, C.C. Toward an integrated coastal sea-ice observatory: System components and a case study at Barrow, Alaska. *Cold Reg. Sci. Technol.* **2009**, *56*, 61–72, doi:10.1016/j.coldregions.2008.12.003. [[CrossRef](#)]
45. Ryan, J.C.; Hubbard, A.; Box, J.E.; Brough, S.; Cameron, K.; Cook, J.M.; Cooper, M.; Doyle, S.H.; Edwards, A.; Holt, T.; et al. Derivation of High Spatial Resolution Albedo from UAV Digital Imagery: Application over the Greenland Ice Sheet. *Front. Earth Sci.* **2017**, *5*, doi:10.3389/feart.2017.00040. [[CrossRef](#)]
46. Whitehead, K.; Hugenholtz, C.H. Applying ASPRS Accuracy Standards to Surveys from Small Unmanned Aircraft Systems (UAS). *Photogramm. Eng. Remote Sens.* **2015**, *81*, 787–793, doi:10.14358/pers.81.10.787. [[CrossRef](#)]
47. Schindler, K. Mathematical Foundations of Photogrammetry. In *Handbook of Geomathematics*; Springer: Berlin/Heidelberg, Germany, 2015; pp. 3087–3103, doi:10.1007/978-3-642-54551-1_63.
48. Carbonneau, P.E.; Dietrich, J.T. Cost-effective non-metric photogrammetry from consumer-grade sUAS: implications for direct georeferencing of structure from motion photogrammetry. *Earth Surf. Process. Landf.* **2016**, *42*, 473–486, doi:10.1002/esp.4012. [[CrossRef](#)]
49. James, M.R.; Robson, S. Mitigating systematic error in topographic models derived from UAV and ground-based image networks. *Earth Surf. Process. Landf.* **2014**, *39*, 1413–1420, doi:10.1002/esp.3609. [[CrossRef](#)]
50. Harwin, S.; Lucieer, A. Assessing the Accuracy of Georeferenced Point Clouds Produced via Multi-View Stereopsis from Unmanned Aerial Vehicle (UAV) Imagery. *Remote Sens.* **2012**, *4*, 1573–1599, doi:10.3390/rs4061573. [[CrossRef](#)]
51. Grayson, B.; Penna, N.T.; Mills, J.P.; Grant, D.S. GPS precise point positioning for UAV photogrammetry. *Photogramm. Rec.* **2018**, *33*, 427–447, doi:10.1111/phor.12259. [[CrossRef](#)]
52. Miao, X.; Xie, H.; Ackley, S.F.; Zheng, S. Object-Based Arctic Sea Ice Ridge Detection From High-Spatial-Resolution Imagery. *IEEE Geosci. Remote Sens. Lett.* **2016**, *13*, 787–791, doi:10.1109/lgrs.2016.2544861. [[CrossRef](#)]
53. Gupta, M. Various remote sensing approaches to understanding roughness in the marginal ice zone. *Phys. Chem. Earth Parts A/B/C* **2015**, *83–84*, 75–83, doi:10.1016/j.pce.2015.05.003. [[CrossRef](#)]
54. Nolin, A.; Mar, E. Arctic Sea Ice Surface Roughness Estimated from Multi-Angular Reflectance Satellite Imagery. *Remote Sens.* **2018**, *11*, 50, doi:10.3390/rs11010050. [[CrossRef](#)]

55. Miao, X.; Xie, H.; Ackley, S.F.; Perovich, D.K.; Ke, C. Object-based detection of Arctic sea ice and melt ponds using high spatial resolution aerial photographs. *Cold Reg. Sci. Technol.* **2015**, *119*, 211–222, doi:10.1016/j.coldregions.2015.06.014. [[CrossRef](#)]
56. Popović, P.; Cael, B.; Silber, M.; Abbot, D.S. Simple Rules Govern the Patterns of Arctic Sea Ice Melt Ponds. *Phys. Rev. Lett.* **2018**, *120*, doi:10.1103/physrevlett.120.148701. [[CrossRef](#)]
57. Hui, F.; Li, X.; Zhao, T.; Shokr, M.; Heil, P.; Zhao, J.; Liu, Y.; Liang, S.; Cheng, X. Semi-Automatic Mapping of Tidal Cracks in the Fast Ice Region near Zhongshan Station in East Antarctica Using Landsat-8 OLI Imagery. *Remote Sens.* **2016**, *8*, 242, doi:10.3390/rs8030242. [[CrossRef](#)]
58. Dammann, D.O.; Eicken, H.; Mahoney, A.R.; Meyer, F.J.; Betcher, S. Assessing Sea Ice Trafficability in a Changing Arctic. *ARCTIC* **2018**, *71*, 59, doi:10.14430/arctic4701. [[CrossRef](#)]
59. McGill, P.; Reisenbichler, K.; Etchemendy, S.; Dawe, T.; Hobson, B. Aerial surveys and tagging of free-drifting icebergs using an unmanned aerial vehicle (UAV). *Deep Sea Res. Part II Top. Stud. Oceanogr.* **2011**, *58*, 1318–1326, doi:10.1016/j.dsr2.2010.11.007. [[CrossRef](#)]
60. Perovich, D.K. Aerial observations of the evolution of ice surface conditions during summer. *J. Geophys. Res.* **2002**, *107*, doi:10.1029/2000jc000449. [[CrossRef](#)]
61. Giles, A.; Massom, R.; Heil, P.; Hyland, G. Semi-automated feature-tracking of East Antarctic sea ice from Envisat ASAR imagery. *Remote Sens. Environ.* **2011**, *115*, 2267–2276, doi:10.1016/j.rse.2011.04.027. [[CrossRef](#)]
62. Hwang, B.; Elosegui, P.; Wilkinson, J. Small-scale deformation of an Arctic sea ice floe detected by GPS and satellite imagery. *Deep Sea Res. Part II Top. Stud. Oceanogr.* **2015**, *120*, 3–20. [[CrossRef](#)]
63. Rosnell, T.; Honkavaara, E. Point Cloud Generation from Aerial Image Data Acquired by a Quadrocopter Type Micro Unmanned Aerial Vehicle and a Digital Still Camera. *Sensors* **2012**, *12*, 453–480, doi:10.3390/s120100453. [[CrossRef](#)] [[PubMed](#)]
64. Turner, D.; Lucieer, A.; Wallace, L. Direct Georeferencing of Ultrahigh-Resolution UAV Imagery. *IEEE Trans. Geosci. Remote Sens.* **2014**, *52*, 2738–2745, doi:10.1109/tgrs.2013.2265295. [[CrossRef](#)]
65. Cucci, D.A.; Rehak, M.; Skaloud, J. Bundle adjustment with raw inertial observations in UAV applications. *ISPRS J. Photogramm. Remote Sens.* **2017**, *130*, 1–12, doi:10.1016/j.isprs.2017.05.008. [[CrossRef](#)]



© 2019 by the authors. Licensee MDPI, Basel, Switzerland. This article is an open access article distributed under the terms and conditions of the Creative Commons Attribution (CC BY) license (<http://creativecommons.org/licenses/by/4.0/>).